

Skin modes in a nonlinear Hatano-Nelson model

Bertin Many Manda,¹ Ricardo Carretero-González,² Panayotis G. Kevrekidis,³ and Vassos Achilleos¹

¹*Laboratoire d'Acoustique de l'Université du Mans (LAUM), UMR 6613,*

Institut d'Acoustique - Graduate School (IA-GS), CNRS, Le Mans Université, France

²*Nonlinear Dynamical Systems Group, Computational Sciences Research Center,*

and Department of Mathematics and Statistics, San Diego State University, San Diego, California 92182-7720, USA

³*Department of Mathematics and Statistics, University of Massachusetts, Amherst, MA 01003-4515, USA*

(Dated: November 16, 2023)

Non-Hermitian lattices with non-reciprocal couplings under open boundary conditions are known to possess linear modes exponentially localized on one edge of the chain. This phenomenon, dubbed non-Hermitian skin effect, induces all input waves in the linearized limit of the system to unidirectionally propagate toward the system's preferred boundary. Here we investigate the fate of the non-Hermitian skin effect in the presence of Kerr-type nonlinearity within the well-established Hatano-Nelson lattice model. Our method is to probe the presence of nonlinear stationary modes which are localized at the favored edge, when the Hatano-Nelson model deviates from the linear regime. Based on perturbation theory, we show that families of nonlinear skin modes emerge from the linear ones at any non-reciprocal strength. Our findings reveal that, in the case of focusing nonlinearity, these families of nonlinear skin modes tend to exhibit enhanced localization, bridging the gap between weakly nonlinear modes and the highly nonlinear states (discrete solitons) when approaching the anti-continuum limit with vanishing couplings. Conversely, for defocusing nonlinearity, these nonlinear skin modes tend to become more extended than their linear counterpart. To assess the stability of these solutions, we conduct a linear stability analysis across the entire spectrum of obtained nonlinear modes and also explore representative examples of their evolution dynamics.

I. INTRODUCTION

Advances in the studies of non-conservative systems using non-Hermitian operators have led to the discovery of various interesting phenomena. At the origin of these research activities lies the seminal work on \mathcal{PT} -symmetry [1, 2] describing systems featuring the simultaneous balance of energy dissipation and gain. \mathcal{PT} -symmetry provides the means to construct non-Hermitian operators, which under certain conditions may support modes with real eigenvalues [3, 4]. These results were confirmed and validated in many different physical domains including optics, acoustics, mechanical, and electrical systems; for a recent review, see e.g., the book [5]. More recently, \mathcal{PT} -symmetry, was also employed in the context of topology and now plays a significant role in the studies of non-Hermitian topology [6, 7]. It is now understood that non-Hermitian topology may substantially differ from its Hermitian counterpart.

Within the context of non-Hermiticity and topology, a new class of models featuring asymmetric (often non-reciprocal) couplings between their constituents have been introduced. Unlike Hermitian or \mathcal{PT} -symmetry systems, it is found that the spectral characteristics of systems with asymmetric (non-reciprocal) couplings greatly vary depending on their boundaries [8–14]. In general, these type of non-Hermitian systems under periodic boundaries possess complex spectra with Bloch-type linear modes. Nevertheless, the same system with open boundary conditions (OBC) may display a real spectrum. More importantly, the eigenmodes under OBC are found to be exponentially localized on one side of the

system. This phenomenon is dubbed the non-Hermitian skin effect (NHSE) and constitutes one of the latest developments in this area; see e.g., Refs [11, 13] for a review. In practice, the skin effect is a manifestation of the asymmetry of the couplings favoring the accumulation of amplitude in one side. Note that most of the properties of the NHSE and of non-Hermitian topology can be understood using the seminal linear Hatano-Nelson (HN) model [15, 16], a non-Hermitian one-dimensional lattice with asymmetric nearest neighbor couplings. The intense interest in this structures has led to several experimental manifestations of the NHSE in optics [17], acoustics [18, 19], mechanics [20, 21], electric circuits [22], and atomic lattices [23].

As is often the case, the phenomena of non-Hermitian and topological systems have been pursued also in the realm of nonlinear waves. On one hand, the study of the interplay between nonlinearity and topology is rapidly expanding, giving rise the new phenomena such as topological breathers and solitons [24–29]. In addition, the interaction between non-Hermiticity and nonlinearity, has been extensively focused mainly on \mathcal{PT} -symmetric systems (see, e.g., the reviews [5, 30, 31]). Even more recently the experiments exploiting the interplay between topology, \mathcal{PT} -symmetry and nonlinearity have been performed [32].

To our knowledge, models featuring asymmetric (non-reciprocal) interactions and the NHSE have been merely studied under the effect of nonlinearity. In fact only few works [33–36] recently appeared with Kerr-type nonlinearities. In particular, Refs. [33, 36] focus on a few site lattice, and at the extreme limit where each lattice site

is only connected to its right (or left) nearest neighbor. In addition, Ref. [34] studied the dynamics of single-site wave-packets at the center of the HN chain, demonstrating that nonlinear NHSEs exist, but may be hindered by self-trapping processes.

Here, we intend to shed more light on the fate of the NHSE of the HN model in the nonlinear regime. To do so we study the HN model with Kerr-type nonlinearity ensuing from a non-reciprocal variant of the discrete nonlinear Schrödinger (DNLS) equation [37]. We thus focus on finding nonlinear skin modes (NLSMs) stemming from the corresponding linear ones. By applying perturbation theory we show that small amplitude NLSMs emerge for all linear modes both with focusing (positive) or defocusing (negative) signs of the nonlinearity. We find families of NLSMs which connect the linear and the strongly nonlinear anticontinuum (AC) limit where the coupling between each site vanishes. We also carry a linear stability analysis and identify regions where NLSMs can be either stable or unstable. Our analysis shows that small perturbations that do not have a skin-like profile will eventually destabilise the NLSMs.

The paper is structured as follows. In Sec. II, we discuss the existence of such NLSMs. In Sec. III, we tackle their stability and dynamics. Finally in Sec. IV, we present our conclusions and a number of directions for future studies. Finally, in the Appendices we provide a number of details regarding our perturbation theory analysis in the different limits.

II. NONLINEAR SKIN MODES

In this work we are interested in finding nonlinear skin modes of the following nonlinear version of the HN model

$$i\frac{d\psi_n}{d\tau} = C(\psi_{n+1} + t\psi_{n-1}) + \sigma|\psi_n|^2\psi_n, \quad (1)$$

where $n = 1, 2, \dots, N$ indexes the lattice sites and ψ_n is a complex-valued amplitude at site n , as shown in Fig. 1(a). Here, C is the (real) hopping (coupling) strength and t is the non-reciprocal parameter: if $t = 1$ the system is reciprocal while for any value $t \neq 1$ there is a preferred direction. We further assume a general Kerr-type (self-interaction) nonlinearity with strength $\sigma = \pm 1$ relevant to many physical systems especially in nonlinear optics [38–40] and cold atomic gases [41, 42], or even biomolecules [43, 44]. Indeed, this model in the $t = 1$ limit constitutes the prototypical nonlinear dispersive dynamical lattice of the DNLS type [37]. Here, we explore a hybrid between this well-established setting and the linear HN model, to examine the interplay of asymmetric dispersion and cubic nonlinearity.

Our goal is to find stationary solutions, with energy E , assuming $\psi_n(\tau) = u_n e^{iE\tau}$ which leads to the following set of nonlinear equations [33, 36]

$$Eu_n = C(u_{n+1} + tu_{n-1}) + \sigma|u_n|^2u_n. \quad (2)$$

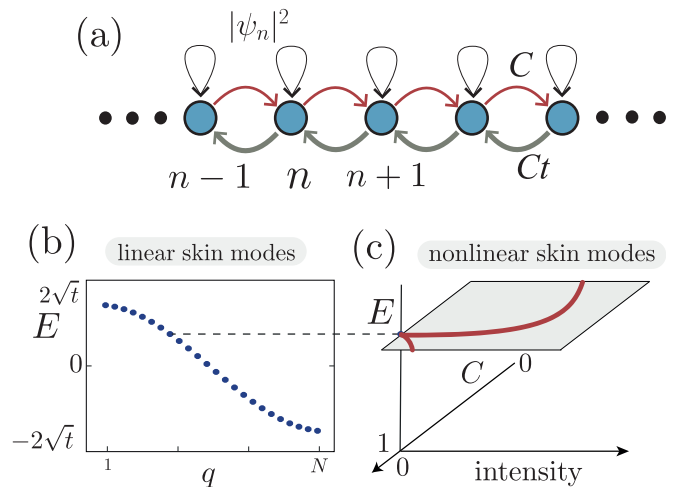


FIG. 1. (a) The proposed nonlinear HN model where closed loops represent the on-site Kerr terms. (b) The linear spectrum of a HN model with with open boundary conditions. (c) An illustration of how a family of nonlinear skin modes emerges from the corresponding linear solution.

The linear HN model (obtained for $\sigma = 0$ and $C = 1$) yields

$$Eu_n = u_{n+1} + tu_{n-1}. \quad (3)$$

For a finite HN lattice with OBC $u_0 = u_{N+1} = 0$, Eq. (3) can be recast in the form of an eigenvalue problem $H\vec{u}_q^{(0)} = E_q\vec{u}_q^{(0)}$ (the expression of H is provided in Appendix A), where the real eigenenergies are equal to

$$E_q = 2\sqrt{t} \cos\left(\frac{q\pi}{N+1}\right), \quad (4)$$

with $q = 1, \dots, N$. An example of such a spectrum is shown in Fig. 1(b) for $N = 24$. The corresponding eigenvectors $\vec{u}_q^{(0)}$ have elements which satisfy the following equation

$$u_{q,n}^{(0)} = \sqrt{\frac{2}{N+1}} t^{n/2} \sin\left(\frac{nq\pi}{N+1}\right). \quad (5)$$

From Eq. (5), it becomes clear that whenever $t < 1$ ($t > 1$) the modes of the HN are localized to the left-(right-) hand side of the lattice owing to the t -dependent prefactor. This is exactly the manifestation of the NHSE which we systematically generalise here in the nonlinear domain. In fact, since the eigenvalue problem is non-Hermitian, there exist also left eigenvectors, \vec{v}_q , satisfying $\vec{v}_q^T H = \vec{v}_q^T E_q$. These left eigenvectors are localized at the opposite side of the lattice. It is worth noting that we normalize these eigenvectors using the bi-orthonormalization, i.e., $\vec{v}_{q'}^T \vec{u}_q^{(0)} = \delta_{q'q}$ [45].

Our main goal is to show that families of NLSMs satisfying Eq. (2) emerge from their linear counterparts for our finite lattices. In particular, we choose to keep the

energy E (i.e., the nonlinear eigenvalue parameter, referred to as propagation frequency in optics and chemical potential in atomic physics) fixed to that of the linear modes, and then numerically obtain solutions by varying the coupling strength, C . A sketch of this procedure and its outcomes is shown in Fig. 1(c). Let us first use the regular perturbation theory (RPT) to show that for any value of $t \neq 0$, small amplitude nonlinear solutions can emerge from each linear mode. To this end, we assume solutions of Eq. (2) in the following asymptotic form

$$u_n = \epsilon u_n^{(0)} + \epsilon^2 u_n^{(1)} + \epsilon^3 u_n^{(2)} + \mathcal{O}(\epsilon^4), \quad (6)$$

where $u_n^{(0)}$ are the linear modes [Eq. (3)]. Since the continuation is performed at constant energy, E_q for each of the modes, C then becomes the continuation parameter that varies in a way such that for sufficiently small amplitude solutions we consider

$$C = 1 + C_1 \epsilon^2 + \mathcal{O}(\epsilon^4). \quad (7)$$

The details of the perturbation theory are found in the Appendix B; here we only present the main results. We find that finite amplitude solutions of the nonlinear eigenvalue problem [Eq. (2)] exist starting from terms of $\mathcal{O}(\epsilon^3)$ with a correction to C given by

$$C_1 = -\frac{\sigma}{E_q} \left(\frac{2}{N+1} \right)^2 \sum_{n=1}^N t^n \sin^4 \left(\frac{nq\pi}{N+1} \right). \quad (8)$$

We note that this expression can be resummed, provided that we decompose the \sin^4 into Fourier modes and consider the resulting geometric series, yet given the intricacy of the resulting expression, we do not explore that step herein. In practice, the above result says that for small amplitudes a family of nonlinear modes emerges from each respective linear mode followed by a change in the coupling parameter C . Furthermore the negative sign in front of Eq. (8) signals the fact that for $\sigma = +1$ (focusing case) the coefficient C decreases as the amplitude grows, while the opposite happens for the defocusing case. In addition we see that the correction C_1 strongly depends on the value of the non-reciprocal parameter t .

A. Focusing regime

To verify the above result, we solve Eq. (2) numerically by fixing E to a linear eigenvalue E_q [Eq. (4)] employing a pseudo-arclength nonlinear solver [46–48]. The initial guess seeded to the solver is the corresponding linear mode rescaled to very small amplitudes. That way the value of C is left as an unknown parameter to be found by the pseudo-arclength solver. In Fig. 2 we show results for the case of the first linear mode ($q = 1$) for a lattice of $N = 24$ oscillators. Figure 2(a) shows the numerically calculated total intensity of the lattice

$$S = \sum_n |u_n|^2, \quad (9)$$

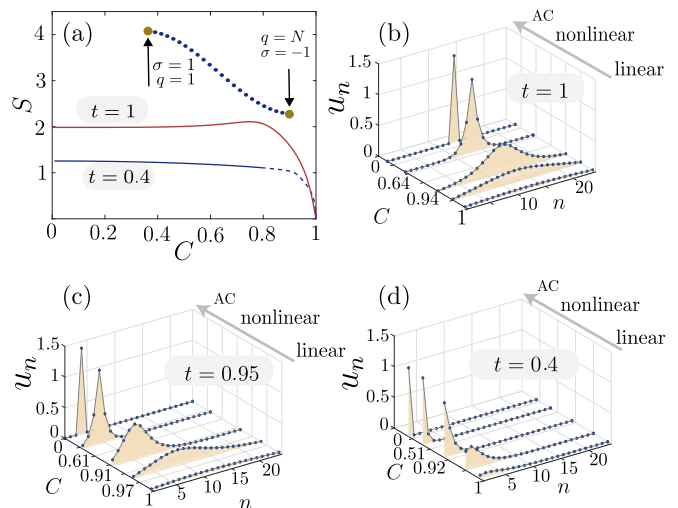


FIG. 2. (a) The total intensity, S , as a function of the coupling strength, C , for the family of nonlinear stationary solutions emerging from the first linear mode with $t = 1$ (red curve) and $t = 0.4$ (blue curve). The dashed regions of the curves indicate linearly unstable solutions. Further, the inset shows the linear spectrum. (b) Representative nonlinear modes of the family with $t = 1$ for different C values. (c) and (d) Same as (b) but for the families of NLSMs with $t = 0.95$ and $t = 0.4$, respectively.

as a function of the coefficient C for two values of t mapping to the usual DNLS equation with $t = 1$ and the nonlinear HN model with $t = 0.4$. As predicted, a family of nonlinear modes emerges from the linear limit with decreasing values of C . In addition, beyond the validity of the perturbation series in the neighborhood of the linear regime, we numerically find that each family terminates at the AC limit, where the oscillators are uncoupled, i.e., $C = 0$. In fact, the existence of this branch bifurcating from the AC limit can also be demonstrated through regular perturbation theory from the latter limit. The details of these calculations are given in Appendix C.

For illustrative purposes, in Fig. 2(b) we show the profile of some solutions for the family with $t = 1$ (corresponding to the DNLS model). Clearly, small amplitude nonlinear solutions are similar to the well-known sinusoidal form of the linear mode in the neighborhood of unit coupling strength. As C decreases away from unity and nonlinearity becomes stronger, these solutions become more localized yet remain spatially symmetric (i.e. the location of their centers of mass does not change) with in-phase amplitudes at adjacent oscillators. At the AC limit ($C = 0$), the corresponding family of modes is connected to a single site solution at the center of the lattice satisfying $E_1 = |u_{N/2}|^2$ [49]. Note that this is a finite size effect in contrast to the well known results for $N \rightarrow \infty$ where single-site solutions in the AC limit are connected to the continuum soliton, as the coupling is increased [37].

Moving away from the DNLS limit, in Fig. 2(c), we dis-

play instances of NLSMs of the HN model with $t = 0.95$. As expected small amplitude solutions remain close to the shape of the linear skin mode. However as the amplitudes grows (C decreases) the center of mass of the obtained modes moves toward the favored direction [for $t < 1$, i.e., to the left side of the chain of Fig. 1(a)]. It follows that focusing nonlinearity not only tends to localize the modes but also strengthens the skin effect. In fact, even for a small deviation from the standard DNLS model in this example ($t = 0.95$), the resulting family of NLSMs connects to the single-site solution located far away from the lattice's center as seen in Fig. 2(c). More importantly, we numerically confirmed that this shifting toward the left becomes stronger as t is further decreased, till the families of NLSMs starting from the first linear mode, end up at a single-site solution in the AC limit, located at the left edge of the chain. This happens for all values of t below the threshold, $t_c \approx 0.57$. Interestingly the t_c happens to be independent of lattice size, at least up to the largest chain ($N = 50$) considered in our numerical simulations. Examples of such a family of NLSMs is shown in Fig. 2(d) for $t = 0.4$. We note in passing the staggering transformation $u_n \rightarrow (-1)^n u'_n$ within Eq. (2), leads to the following

$$-Eu'_n = C(u'_{n+1} + tu'_{n-1}) - \sigma|u'_n|^2 u'_n. \quad (10)$$

Consequently, if (E, u_n, σ) is a solution of the nonlinear eigenvalue problem, then $(-E, u'_n, -\sigma)$ is also a solution. As such the families of NLSMs generated through the linear mode of wave number $q' = N + 1 - q$ with $\sigma = -1$ overlaps with the ones arising from the linear mode with index q , fixing $\sigma = 1$; see the inset of Fig. 2(a).

Let us now look for families of NLSMs stemming from linear modes of higher wave number. The S vs. C plot resulting from the numerical continuations is shown in the panels of Fig. 3 using as initial guess the linear modes of wave numbers $q = 2$ [Fig. 3(a)] and $q = 5$ [Fig. 3(e)], considering two different values of the strength of non-reciprocity with $t = 0.2$ (blue curves) and $t = 0.6$ (red curves). Similarly to Fig. 2 these families join the linear regime at $C = 1$ with the AC limit of $C = 0$. Focusing now on the shapes of the resulting NLSMs, we find that they inherit the number of nodes pertaining to the order of the mode in the linear counterpart. Namely, the 2nd mode results in a 2-site state, the 5th mode to a 5-site one, etc. Given their excited nature, the resulting NLSMs are also “twisted” (i.e., corresponding to alternating, out-of-phase, field values) [37, 50]. These NLSMs also tend to shift toward the preferred direction of the system at high intensity, see e.g., Figs. 3(b) and (c). As such, the shape of the high amplitude NLSMs, greatly differs from the linear one. In particular, for the examples in Figs. 3(b) and (c) and Fig. 3(e) and (f) the shape of these high amplitude NLSM becomes closer to the 2-site and 5-site stationary solutions of the AC limit, respectively for families emerging from the second [Figs. 3(b) and (c)] and fifth [Figs. 3(e) and (f)] linear modes. It is important to emphasize that from our simulations, we

conjecture that the q -th linear mode of unit coupling is connected to a q -site solution in the AC limit, with out-of-phase excited oscillators. The latter, as was illustrated for $t = 1$ in Ref. [50] and as follows from the calculations in Appendix B for $t \neq 1$, are spectrally stable states near the AC limit.

Interestingly, the location of the excited oscillators at the AC limit depends on the strength of the non-reciprocity, t . Namely, at the $t = 1$ (DNLS) limit, we expect the positions of the excited oscillators to be equally spaced inside the bulk of the chain due to the symmetry of the model. However, when $t \neq 1$, we have seen in Fig. 2, that the NHSE tends to shift the positions of these excited oscillators *independently* toward the most favorable direction of wave propagation within the lattice. This can be clearly seen when comparing the families emerging from the second linear modes at $t = 0.6$ and $t = 0.2$ respectively in Fig. 3(b) and Fig. 3(c). The former features excited oscillators with indices $n = 1$ and $n = 4$ [Fig. 3(b)], while the latter ones with $n = 1$ and $n = 2$ [Fig. 3(c)] at $C = 0$. A similar observation can be drawn from Figs. 3(e) and 3(f), where the larger t can afford the separation of the excited sites by empty “holes”, while for the lower t , these holes are suppressed in favor of the adjacent excitation of all the nonzero nodes at the AC limit. Furthermore, we computed the critical strength of non-reciprocity, t_c below which families of NLSMs emerging from the linear modes connect to consecutive excited oscillators in the AC limit. We obtain that t_c is independent on the lattice size, and has values $t_c \approx 0.25$ for $q > 1$, in line with the results of Fig. 3.

B. Defocusing regime

It is also worth discussing the defocusing case ($\sigma = -1$). According to the regular perturbation theory and especially Eq. (8), families of NLSMs with increasing C can emerge from the linear limit with defocusing nonlinearity, i.e., for $\sigma = -1$. This is confirmed by our numerical simulations. In Fig. 4(a) we depict the total intensity as a function of the coupling strength for selected numbers of families of NLSMs arising from the linear modes with index $q = 1$, $q = 5$, $q = 9$ and $q = 12$ for the case $t = 0.4$. For these solutions the total intensity S grows monotonically with respect to C without showing any sign of saturation, in contrast to what is seen in the focusing case; see gray curves of Fig. 4(a).

Figure 4(b) depicts representative NLSMs of the family emerging from the first linear mode with $t = 0.4$. A direct comparison of these results can be carried with respect to the focusing case in Fig. 2(d). It follows that, contrary to what is seen in the focusing regime, in the defocusing case, the linear skin mode tends to widen as the total intensity of the system grows. This is in line with the defocusing nature of the nonlinearity which apparently dominates the NHSE of the corresponding linear problem for the $q = 1$ state. This increase in width of

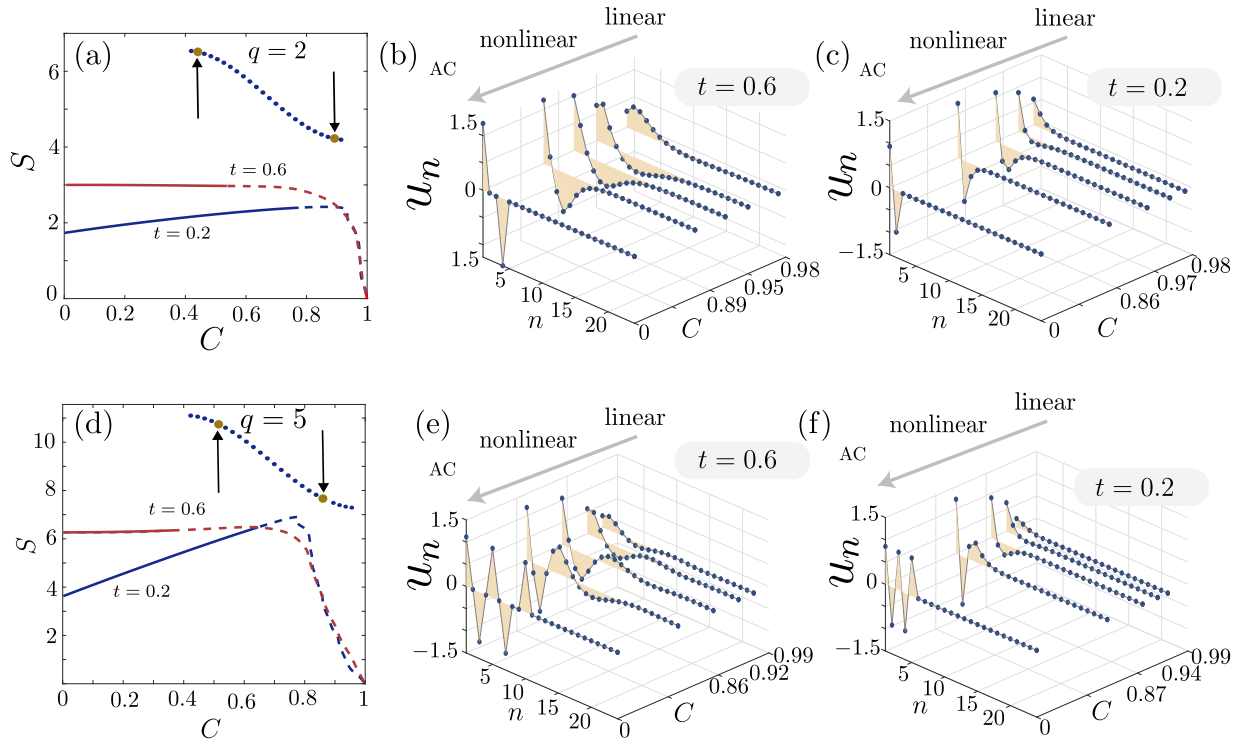


FIG. 3. (a) Intensity S as a function of C for the family of NLSMs originating from the second linear mode at two different values of t with $t = 0.2$ and $t = 0.6$. Note that solid vs. dashed reflects the stable vs. unstable branches; also, note that additional branches to the ones originating from the linear limit are depicted in this panel (see details in the text). (b) Representative profile of the NLSM associated with the family originating from the second linear mode with $t = 0.6$, red curve in (a). (c) Same as in (b), but for $t = 0.2$, blue curve in (a). (d) Same as (a), but for the families of NLSMs emerging from the fifth linear mode. (e) Same as (b) but for (d). (f) Same as (c) but for (d).

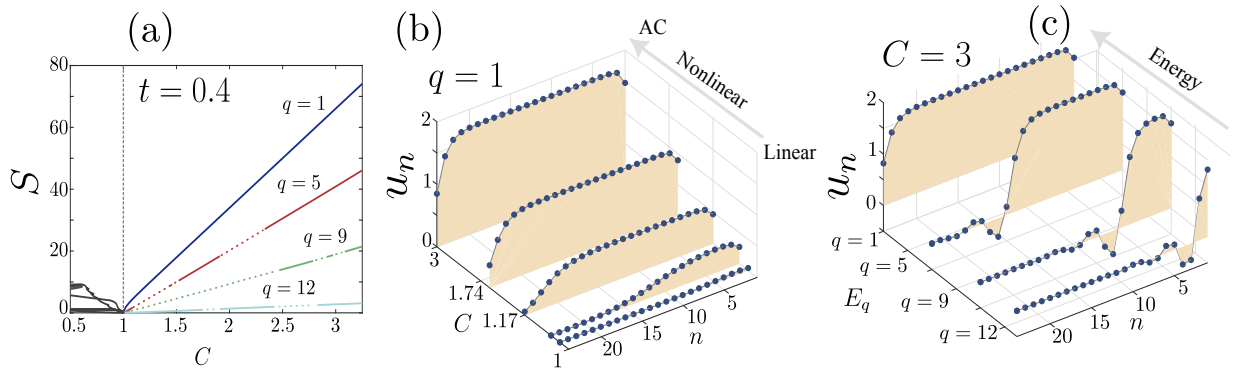


FIG. 4. (a) Total intensity, S against C for the full families of stationary states emerging from the linear modes with $q = 1$, $q = 5$, $q = 9$, and $q = 12$ at constant E for $t = 0.4$. Dotted regions represent unstable NLSMs. (b) Five representative NLSMs of the family emerging from the first linear mode at different coupling strengths. (c) Same as (b), but at fixed value of C with different energies.

the NLSMs, leads to almost extended nonlinear states at high amplitude. Nevertheless, we find that such extended states are not reached for all linear mode energies. In fact, the families of NLSMs arising from linear skin modes of higher wave number display clear localization at the edge of the chain even for high amplitude states. In fact, by fixing the value of C and comparing NLSMs of increasing q we find that their width tends to decay as

shown for example in Fig. 4(c). Additionally, an interesting feature of an oscillatory tail can be seen to develop for this panel's case of $C = 3$. As this regime is far from the regime accessible to perturbative analysis, we do not pursue this feature further.

III. STABILITY AND DYNAMICS

For a complete study of the NLSMs we need to study their stability under the effect of small perturbations. Such a linear stability analysis is typical for the DNLS model and is usually performed substituting the ansatz $\bar{\psi}(\tau) = (\bar{u} + \epsilon\bar{w}(\tau))e^{iE\tau}$ into Eq. (1) with \bar{u} being the numerically obtained NLSM and $\epsilon\bar{w}$ a small perturbation. By expressing the elements of the perturbation vector as $w_n(\tau) = a_n e^{i\lambda\tau} + b_n^* e^{-i\lambda^*\tau}$, where the asterisk denotes the complex conjugate, we end up with the following eigenvalue problem [50]

$$JL \begin{pmatrix} \bar{a} \\ \bar{b} \end{pmatrix} = \lambda \begin{pmatrix} \bar{a} \\ \bar{b} \end{pmatrix}, \quad (11)$$

where we represent the stability matrix $Z \equiv JL$ as a product of two matrices: J the symplectic matrix and L a linearization matrix which depends on the stationary state u_n and acts on the spatial part of the perturbation eigenvector w_n (further details are in Appendix A). A NLSM is said to be linearly stable if the eigenvalues λ of Z are real. The matrix J is skew symmetric while $L^T \neq L$ is generally non-Hermitian for $t \neq 1$. However by using the similarity transformation $\tilde{L} = D^{-1}LD$ we can show that $\tilde{L}^T = \tilde{L}$. Here, using $D = \text{diag}(d_0, d_1, \dots, d_{N-1}, d_0, d_1, \dots, d_{N-1})$ with elements $d_n = \sqrt{t^n}$, $n = 0, \dots, N-1$ allows us to rewrite the stability eigenvalue problem [Eq. (11)] as follows

$$J\tilde{L} \begin{pmatrix} \tilde{a} \\ \tilde{b} \end{pmatrix} = \lambda \begin{pmatrix} \tilde{a} \\ \tilde{b} \end{pmatrix}, \quad (12)$$

where $\tilde{a} = D^{-1}\bar{a}$ and $\tilde{b} = D^{-1}\bar{b}$. It follows that the matrix product $J\tilde{L}$ is real and symplectic. Thus the eigenvalues of the stability problem [Eq. (11)] come in quartets $\lambda, \lambda^*, -\lambda$ and $-\lambda^*$.

In Fig. 2(a), Fig. 3(a) and Fig. 4(a), the S against C dependence of the representative families of NLSMs also displays the results of their linear stability analysis. Namely, we mark stable regions by bold (colored) curves, otherwise unstable. In the focusing case, we find that the NLSMs are stable in the vicinity of the linear regime as depicted in Fig. 7 of Appendix B. The same applies in the neighborhood of the AC limit, whose stable nature is well shown in Fig. 2(a), Fig. 3(a) and Fig. 8. These two regions of stability typically sandwich unstable regions of NLSMs with moderate (and/or high) intensity [see e.g., Fig. 2(a) and Fig. 3(a)].

Regarding the eigenspectrum of the stability matrix, representative cases are shown for a stable [Fig. 5(a)] and complex (oscillatory) unstable [Fig. 5(b)] NLSMs of the family emerging from the second linear mode with $t = 0.6$, see the red curve in Fig. 3(a). The stable mode is taken at $C = 0.501$ and the unstable one at $C = 0.527$. In addition, in Fig. 5(c), we depict the eigenvectors associated with the eigenvalues of Fig. 5(b) sorted by increasing value of the participation

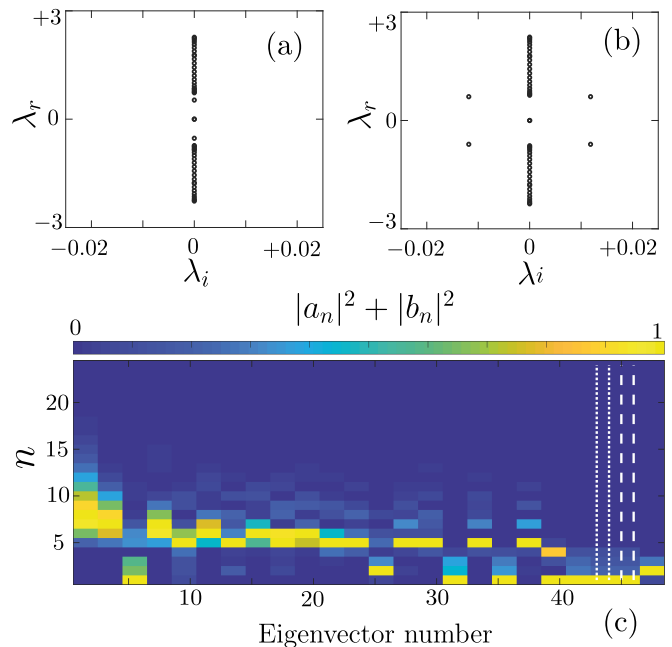


FIG. 5. Eigenvalues λ of the linear stability problem for the stationary solutions with (a) $C = 0.501$ and (b) $C = 0.527$ of the family of NLSMs emerging from the second skin linear mode at constant energy, red curve in Fig. 3(a). (c) Amplitude, $|a_n|^2 + |b_n|^2$, of the eigenvectors of the eigenvalues in panel (b) sorted by decreasing participation number (see text for details). For clarity, the amplitudes are rescaled by the maximum at each eigenvector. The dotted and dashed line indicates the most unstable eigenvectors associated with eigenvalues with the largest positive and negative imaginary parts respectively [see panel(b)].

number $(\sum_k |a_k|^2 + |b_k|^2)^2 / \sum_n (|a_n|^2 + |b_n|^2)^2$. These eigenvectors come in pairs and display “skinny”-like profiles which are a clear manifestation of the features of the HN model. Furthermore, this can be used to represent the generic form of a perturbation through which the linear stability of the NLSMs is defined.

To confirm the stability analysis, we numerically solve the equations of motion [51–53] of the HN chain [Eq.(1)] using an initial condition of the form $\bar{\psi}(\tau = 0) = \bar{u} + \epsilon\bar{w}(\tau = 0)$ where u_n is the numerically obtained NLSM and $w_n(\tau = 0) = a_n + b_n$ an initial deviation vector with unit norm. Furthermore, we set $\epsilon = 3 \times 10^{-3}$. The time evolution of the *stable* NLSM of Fig. 5(a) perturbed along the direction of one of the eigenvectors of its stability matrix is shown in Fig. 6(a). As expected the mode preserves its shape throughout the whole numerical integration. Repeating the same procedure with the unstable NLSM in Fig. 5(b) of the same family, eventually we observe that it deforms its shape as shown in Fig. 6(b). In fact, we see that after the instability sets in, the total intensity of the field grows substantially, while the state remains localized at the edge of the lattice at all times. It follows from the above that the total intensity S [Eq. (9)] is not preserved during the time evolution.

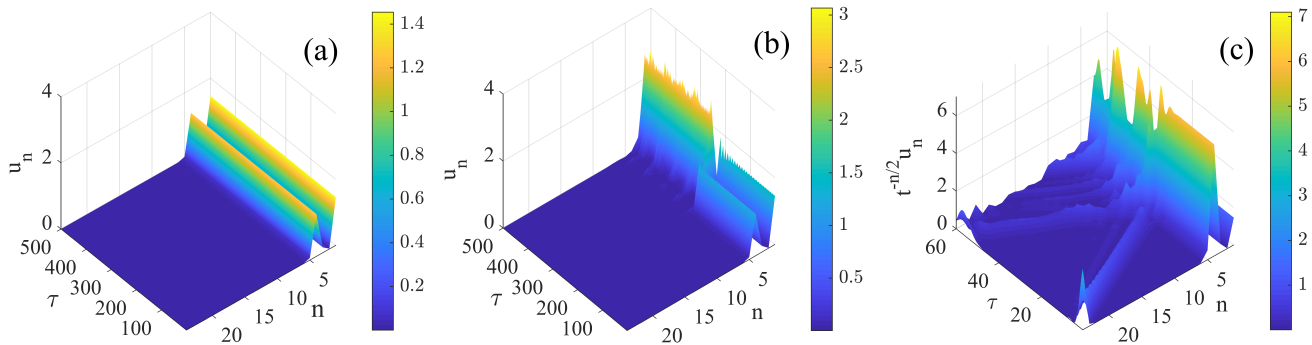


FIG. 6. Nonlinear HN lattice dynamics. The initial conditions $\psi_n(\tau = 0) = u_n(\tau = 0) + \epsilon w_n(\tau = 0)$ with $\epsilon = 3 \times 10^{-3}$ and $|\vec{w}| = 1$. (a) Stable NLSM, $u_n(\tau = 0)$, with $C = 0.501$ and $t = 0.6$ from the family of the second ($q = 2$) linear mode (see Fig. 3) with perturbation $w_n(\tau = 0) = a_n + b_n$ constructed with a random sum of eigenvectors of the stability matrix $Z = JL$ [Eq. (11)]. (b) Unstable NLSM, $u_n(\tau = 0)$, with $C = 0.527$ and $t = 0.6$ belonging to the same branch as in panel (a) with perturbation $w_n(\tau = 0)$ corresponding to the eigenvector of Z along the most unstable direction. (c) Same as in (a), but for $w_n(\tau = 0) = (0, 0, 0, \dots, 0, e^{i\kappa_N})$, with $\kappa_N = 2.727$ being randomly drawn from $[-\pi, \pi]$. Note that we have verified that the result of (c) is representative of the dynamics of perturbations with different realizations of the random phase.

Nevertheless, the transformed quantity $S_D = \sum_n t^n |u_n|^2$ is an integral of motion, such that these amplitudes are bounded as long as the lattice is finite.

Similar stability results are also found for the defocusing case. The exception here consists of the family of NLSMs arising from the first mode which are always stable as shown by the blue curve in Fig. 4(a). In fact, these states are known to act as ground states for the chain, since they minimize the energy functional of the system [54], as is typically the case in such self-defocusing settings (both continuum and discrete).

We now finish this section with a dynamical observation regarding the choice of perturbation in the results of the linear stability. It is crucial to note that the stability analysis is valid as long as we perturb the system with skin-like deviations, $\vec{w}(\tau = 0)$ as the ones used in Figs. 6(a) and (b). Without loss of generality, a simple counter example is a perturbation of an otherwise stable NLSM, \vec{u} , by a deviation vector $\vec{w}(\tau = 0) = (0, 0, \dots, e^{i\kappa_N})^T$, with κ_n being a random phase uniformly drawn in the interval $[-\pi, \pi]$. The time evolution of this perturbed initial condition $\vec{\psi}(\tau = 0) = \vec{u} + \epsilon \vec{w}$ is shown in Fig. 6(c) for the stable NLSM of Fig 6(a) and Fig. 5(a). Since this is a stable NLSM, one would expect its dynamics to be straightforwardly robust, similarly, e.g., to Fig. 6(a). However, for the choice of perturbation \vec{w} , we observe that the shape of the initial NLSM is greatly modified and after evolving has moved away from the initial stationary mode.

To understand the origin of this outcome, for small ϵ , we need to project the perturbation $\vec{w} = (0, 0, \dots, 1)^T$ into the linear modes of the HN chain, $\vec{w} = \sum_q c_q \vec{u}_q^{(0)}$, following the biorthogonal framework. It follows that the coefficient $c_q = \vec{v}_q^{T(0)} \vec{w} = t^{-N/2}$ with $q = 1, \dots, N$. In the example above, we find that $c_q \sim 450$, such that the perturbation strongly excites all linear modes. Consequently, the amplitude of $\vec{w}(\tau = 0)$ exponentially grows

in time, while its center of mass shifts leftward due to the NHSE. As this perturbation moves to the opposite end of the domain where the NLSM is localized, it interacts with the latter, driving the system away from the orbit of the initially stable skin state as seen in Fig. 6(c) as time evolves. Thus, in this nonlinear HN model, finite perturbations on the “wrong side” of the domain may have detrimental effects through their interaction even with stable NLSMs.

IV. CONCLUSIONS AND FUTURE CHALLENGES

We have analytically predicted and numerically obtained families of nonlinear skin modes (NLSMs) for the non-reciprocal Hatano-Nelson model in the presence of the Kerr nonlinearity. For the case of focusing nonlinearity these modes inherit the property of their linear counterparts and are localized on the preferred side of the lattice. More particularly, in this case, nonlinearity is in synergy with non-reciprocity and it tends to make the modes even more localized than their linear skin counterparts. Furthermore, we show that the families of NLSMs emerging from the linear limit, terminate at the nonlinear extreme of the anticontinuum limit where the coupling between sites vanishes. The analysis of the stability of the modes near the two limits enables us to characterize their respective stability characteristics and corresponding eigenvalues. It also allows us to formulate a perturbation theory framework near these limits. For sufficiently strong non-reciprocity we find that the q th family of NLSM will end up in a configuration of q out-of-phase sites in the anticontinuum limit. These sites may have holes between them if t is sufficiently large, while they become consecutive for values of t that are below a critical threshold. Regarding the defocusing case, we have found nonlinear solutions which are still skinny but, however,

tend to grow in width as the nonlinearity increases. The solution in this regime corresponding to $q = 1$ is found to always be stable, and at high amplitudes it tends to occupy all the (finite) lattice. In addition to the existence and stability, we have also explored the dynamics of the corresponding modes and have shown how the instabilities (e.g., associated with complex eigenvalue quartets) manifest themselves, as well as the somewhat unusual (for Hermitian lattices) nature of the impact of a perturbation at the opposite end to that favored (towards localization) by the value of the non-Hermitian parameter t .

While we have provided a systematic analysis of the linear and the anti-continuum modes of the system, various questions still remain to be addressed. A detailed analysis of the nonlinear modes from the anticontinuum limit and their continuation is worthy of further exploration (cf. [50]). Dynamically, the modes that emerge from that limit may not only feature linear (spectral, exponential) instabilities at shorter times, but have been also shown to manifest nonlinear (power-law) instabilities at longer times in the Hermitian case [55]. It would be worthwhile to explore if such instabilities are present in the Hatano-Nelson model. Finally, all of our analysis has been performed in the one-dimensional setting, but such models (in their Hermitian form) are well-known to have intriguing features, such as (discrete) vortical patterns purely in higher-dimensional settings [37], hence the impact of the non-Hermitian nature on such features would also be another important direction to explore. Such directions are currently under consideration and will be presented in future publications.

ACKNOWLEDGMENTS

We express our gratitude to Uwe Thiele for his valuable comments. Financial support for V.A. and B.M.M. was provided by the *Etoiles Montantes en Pays de la Loire* program, within the framework of the NoHENA project. We acknowledge the support from the US National Science Foundation under Grants No. PHY-2110038 (R.C.G.) and No. PHY-2110030 (P.G.K.).

Appendix A: Dynamical and stability matrices of the Hatano-Nelson model

The explicit expression of the dynamical matrix of the Hatano-Nelson (HN) lattice model derived from Eq. (3) with open boundary conditions, i.e. $u_0 = u_{N+1} = 0$, yields

$$H = \begin{pmatrix} 0 & 1 & 0 & 0 & \dots & 0 & 0 \\ t & 0 & 1 & 0 & \dots & 0 & 0 \\ 0 & t & 0 & 1 & \dots & 0 & 0 \\ \vdots & \vdots & \vdots & \vdots & \ddots & \vdots & \vdots \\ 0 & 0 & 0 & 0 & \dots & t & 0 \end{pmatrix}, \quad (\text{A1})$$

for unit hopping strength, $C = 1$, and parameter of non-reciprocity, $t \in [0, 1)$, between adjacent sites. When nonlinearity is introduced in the HN model, we find the nonlinear solutions u_n at energy E by solving Eq. (2) and investigate their stability. The dynamics of small perturbation, w_n from a reference nonlinear state, u_n at energy E , is generated by its so-called stability matrix,

$$Z = \begin{pmatrix} E - 2g|u_1|^2 & -C & 0 & \dots & 0 & 0 & -g(u_1)^2 & 0 & \dots & 0 & 0 & 0 \\ -Ct & E - 2g|u_2|^2 & -C & \dots & 0 & 0 & 0 & -g(u_2)^2 & \dots & 0 & 0 & 0 \\ 0 & -Ct & E - 2g|u_3|^2 & \dots & 0 & 0 & 0 & 0 & \dots & 0 & 0 & 0 \\ \vdots & \vdots & \vdots & \ddots & \vdots & \vdots & \vdots & \vdots & \ddots & \vdots & \vdots & \vdots \\ 0 & 0 & 0 & \dots & -Ct & E - 2g|u_N|^2 & 0 & 0 & \dots & 0 & 0 & -g(u_N)^2 \\ g(u_1)^2 & 0 & 0 & \dots & 0 & 0 & -E + 2g|u_1|^2 & C & \dots & 0 & 0 & 0 \\ 0 & g(u_2)^2 & 0 & \dots & 0 & 0 & Ct & -E + 2g|u_2|^2 & \dots & 0 & 0 & 0 \\ \vdots & \vdots & \vdots & \ddots & \vdots & \vdots & \vdots & \vdots & \ddots & \vdots & \vdots & \vdots \\ 0 & 0 & 0 & \dots & 0 & g(u_N)^2 & 0 & 0 & \dots & 0 & Ct & -E + 2g|u_N|^2 \end{pmatrix}. \quad (\text{A2})$$

The Z is a $2N \times 2N$ matrix, with N denoting the total number of sites of the HN chain. We rewrite this stability matrix in terms of the product of two operators, $Z = JL$, where

$$J = \begin{pmatrix} 0 & I_N \\ -I_N & 0 \end{pmatrix} \quad (\text{A3})$$

stands for the symplectic matrix, with I_N being the $N \times N$ identity matrix and

$$L = J^{-1}Z, \quad (\text{A4})$$

which depends on the state u_n .

Appendix B: Regular perturbation theory: Linear limit

In this section we perform the RPT in the vicinity of the linear regime ($C = 1$) looking at the bifurcation of the linear modes when the coupling strength C is varied. We expand the coupling strength as:

$$C = 1 + \sum_n C_n \epsilon^{2n} = 1 + C_1 \epsilon^2 + \mathcal{O}(\epsilon^4), \quad (\text{B1})$$

in order to retrieve the linear problem at $\epsilon = 0$. The choice of this ansatz is based on the fact that by exam-

ining the signs of the coefficients C_n gives the direction followed by the bifurcation branch. In addition, we also expand the solution using

$$u_n = \sum_k \epsilon^k u_n^{(k-1)} = \epsilon u_n^{(0)} + \epsilon^2 u_n^{(1)} + \epsilon^3 u_n^{(2)} + \mathcal{O}(\epsilon^4). \quad (\text{B2})$$

Thus, as $\epsilon \rightarrow 0$, the amplitude at site n vanishes. Substituting these expressions into the time-independent HN equations

$$Eu_n = C(u_{n+1} + tu_{n-1}) + |u_n|^2 u_n, \quad (\text{B3})$$

leads to

$$\begin{aligned} \epsilon E(\vec{u}^{(0)} + \epsilon \vec{u}^{(1)} + \epsilon^2 \vec{u}^{(2)}) &= \epsilon H \vec{u}^{(0)} \\ &+ \epsilon^2 H \vec{u}^{(1)} + \epsilon^3 \vec{u}^{(2)} + C_1 \epsilon^3 \vec{u}^{(0)} \\ &+ \sigma \epsilon^3 \Gamma[\vec{u}^{(0)}] \vec{u}^{(0)} + \mathcal{O}(\epsilon^4), \end{aligned} \quad (\text{B4})$$

where H and Γ are the dynamical matrix of the HN model and diagonal matrix with non-zero elements $\Gamma_{jj} = |u_j^{(0)}|^2$, respectively. Considering $E = E_q$ i.e. the q -th eigenvalue of H and collecting terms in ϵ in Eq. (B4), it follows that for the first two orders:

$$\begin{aligned} \epsilon^1: E_q \vec{u}_q^{(0)} &= H \vec{u}_q^{(0)}, \\ \epsilon^2: E_q \vec{u}_q^{(1)} &= H \vec{u}_q^{(1)}. \end{aligned} \quad (\text{B5})$$

Eqs.(B5) are satisfied if $\vec{u}_q^{(0)}$ and $\vec{u}_q^{(1)}$ are solutions of the linear HN model. Consequently, $\vec{u}_q^{(1)}$ does not contribute to the amplitude correction of the nonlinear solutions. This correction in amplitude starts to be observed at order $\mathcal{O}(\epsilon^3)$, leading to the non-trivial equations

$$E_q \vec{u}_q^{(2)} = H \vec{u}_q^{(2)} + C_1 H \vec{u}_q^{(0)} + \sigma \Gamma \vec{u}_q^{(0)}. \quad (\text{B6})$$

Multiplying this equation with the left eigenvector $\vec{v}_{q'}$ leads to

$$C_1 = -\sigma \frac{\vec{v}_{q'}^T \Gamma[\vec{u}_q^{(0)}] \vec{u}_q^{(0)}}{E_q \vec{v}_{q'}^T \vec{u}_q^{(0)}} \quad (\text{B7})$$

where we assume the biorthonormalization $\vec{v}_{q'}^T \vec{u}_q^{(0)} = \delta_{q,q'}$ for this derivation. The full expression of C_1 is shown in Eq. (8). We find that focusing nonlinearity leads to decreasing values of C , while the opposite holds for the defocusing case.

Figure 7 shows, in the focusing case ($\sigma = +1$), the results of the comparison of the families of NLSMs bifurcating from the first linear modes for various t values obtained using numerical (bold colored curves) and RPT (black curves). The plot displays the dependence of the total intensity as a function of the coupling strengths for these families and shows a good agreement between the two results for small amplitude waves. As expected, the deviation (slowly) increases as we depart from the unit coupling limit, given the strong dependence of S on C . Furthermore, we also find that the amplitude of these weakly nonlinear states grows faster for strongly non-reciprocal chains compared to the ones with $t \rightarrow 1$; see the inset of Fig. 7.

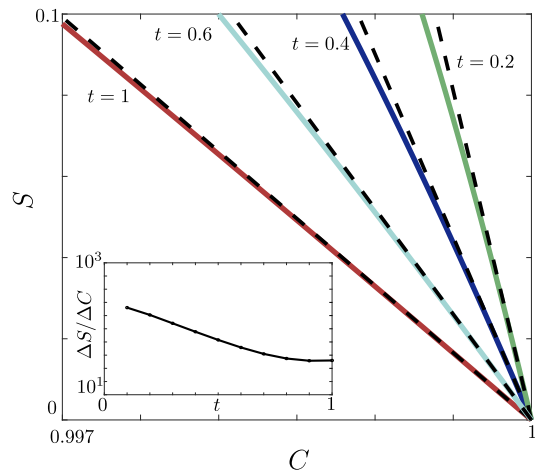


FIG. 7. Total intensity against C for families of NLSMs emerging from the first linear mode for four values of t with $t = 0.2$, $t = 0.4$, $t = 0.6$, and $t = 1$. Note that in the depicted region (namely, close to the linear limit) all branches correspond to *stable* NLSMs. The dashed curves represent the analytical predictions based on the RPT in the neighborhood of the linear skin modes. The inset shows the results of the computation of the rate of growth $\Delta S/\Delta C$ as function of t .

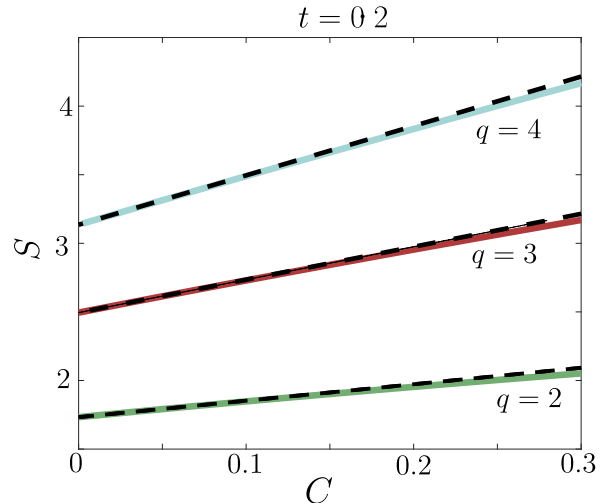


FIG. 8. Same as in Fig. 7, but for families emerging, near the AC (rather than the linear) limit, from the second ($q = 2$), third ($q = 3$) and fourth ($q = 4$) linear skin modes with $t = 0.2$. Note that in the depicted region (namely, close to the anticontinuum limit) all branches correspond to *stable* NLSMs. The dashed lines represent the analytical predictions based on the RPT in the vicinity of the AC limit.

Appendix C: Regular perturbation theory: Anticontinuum limit

We now apply the RPT to show the existence and stability of high amplitude NLSMs when the coupling strength is varied from the AC ($C = 0$) limit [37, 50, 56]. Without loss of generality, we focus here on the so-called

lower order solutions, which arise from initially compact (localized) states of arbitrary size (width) with $M > 2$ at the AC limit. Such NLSMs belong to the families emerging from the linear modes with $t < t_c$, in line with what was discussed in the main text. Assuming the ansatz,

$$\begin{aligned} C &= \beta + \mathcal{O}(\beta^2), \\ u_n &= \tilde{u}_n^{(0)} + \beta \tilde{u}_n^{(1)} + \mathcal{O}(\beta^2), \end{aligned} \quad (\text{C1})$$

where $\beta \ll 1$, and substituting it into the time-independent nonlinear HN equations

$$Eu_n = C(u_{n+1} + tu_{n-1}) + |u_n|^2 u_n, \quad (\text{C2})$$

we obtain,

$$\begin{aligned} E(\tilde{u}_n^{(0)} + \beta \tilde{u}_n^{(1)}) &= \beta(\tilde{u}_{n+1}^{(0)} + t\tilde{u}_{n-1}^{(0)} + \beta \tilde{u}_{n+1}^{(1)} + t\beta \tilde{u}_n^{(1)}) \\ &+ \left[|\tilde{u}_n^{(0)}|^2 + 2\beta \tilde{u}_n^{(0)} \tilde{u}_n^{(1)} \right] \left[\tilde{u}_n^{(0)} + \beta \tilde{u}_n^{(1)} \right] + \mathcal{O}(\beta^2). \end{aligned}$$

Neglecting the $\mathcal{O}(\beta^2)$ and collecting the terms in series of β leads to

$$E\tilde{u}_n^{(0)} = |\tilde{u}_n^{(0)}|^2 \tilde{u}_n^{(0)}, \quad (\text{C3})$$

at order $\mathcal{O}(\beta^0)$. These constitute the discrete equations of the chain at the AC limit for which oscillators are independent. As such, the stationary solutions are well known

$$\tilde{u}_n^{(0)} = \sqrt{E} e^{i\theta_n}, \quad (\text{C4})$$

for the excited (finitely many) sites, while at this leading order the remaining nodes have $\tilde{u}_n^{(0)} = 0$. Furthermore, since we focus on real solutions, we impose the phase $\theta_n = 0, \pi$, which automatically satisfies the corresponding (mass) flux conditions [50].

For the order $\mathcal{O}(\beta^1)$, we have

$$E\tilde{u}_n^{(1)} = (\tilde{u}_{n+1}^{(0)} + t\tilde{u}_{n-1}^{(0)}) + 3|\tilde{u}_n^{(0)}|^2 \tilde{u}_n^{(1)}. \quad (\text{C5})$$

This expression further reduces to

$$-2E\tilde{u}_n^{(1)} = (\tilde{u}_{n+1}^{(0)} + t\tilde{u}_{n-1}^{(0)}), \quad (\text{C6})$$

when considering Eq. (C3). Since we are interested in NLSMs, we can assume that the initial guess at the AC limit is located at the left edge of the chain. Consequently, we write the explicit expression of the first order

correction in amplitude:

$$\begin{aligned} \tilde{u}_1^{(1)} &= -\frac{e^{-i\theta_1}}{2\sqrt{E}} \cos(\theta_2 - \theta_1), \\ \tilde{u}_n^{(1)} &= -\frac{e^{-i\theta_n}}{2\sqrt{E}} [\cos(\theta_{n+1} - \theta_n) + t \cos(\theta_{n-1} - \theta_n)], \\ \tilde{u}_M^{(1)} &= -\frac{e^{-i\theta_M}}{2\sqrt{E}} t \cos(\theta_{M-1} - \theta_M), \end{aligned}$$

with $n = 2, \dots, M-1$. Clearly, the amplitude of the first order correction is $\tilde{u}_n^{(1)}$ and it is inversely proportional to \sqrt{E} . On the other hand, the presence of non-reciprocity through t , induces a symmetry breaking at finite coupling.

Having obtained the different high amplitude NLSMs near the AC limit, we further proceed to characterize their stability. This is done by calculating the largest eigenvalues λ of the stability matrix, Z [Eq. (A2)] using as reference states the nonlinear states of the RPT above. This yields

$$\lambda^2 = 2E\beta\gamma^{(1)}, \quad (\text{C7})$$

with $\gamma^{(1)}$ being the first order correction of the largest eigenvalues of M from the AC limit which depends on the number of excited oscillators, M . Here, we report the results for the two- ($M = 2$) and three- ($M = 3$) site NLSMs. It follows that for $M = 2$,

$$\gamma^{(1)} = (1+t)c_1, \quad (\text{C8})$$

while for the case with $M = 3$,

$$\begin{aligned} \gamma_{\pm}^{(1)} &= \frac{1}{2} \left\{ (1+t)(c_1 + c_2) \right. \\ &\left. \pm \sqrt{(1+t)^2 [c_1^2 + c_2^2] - 2(1+t^2)c_1c_2} \right\} \end{aligned} \quad (\text{C9})$$

where $c_n \equiv \cos \Delta\theta_n$ and $\Delta\theta_n = \theta_n - \theta_{n-1}$. For the families arising from the linear modes we have $\Delta\theta_n = \pm\pi$ which, in turn, can be seen to lead these high amplitude NLSMs to be generically stable near the AC-limit, similarly to their Hermitian counterparts [37].

Figure 8 shows the dependence of the total intensity on the coupling strength for the families emerging from the second, third and fourth linear skin modes at $t = 0.2$. In the neighborhood of the AC limit, it is clear that there is good agreement between the RPT (black curves) and the numerical continuations (colored curves). Furthermore, the stability of these high intensity NLSMs calculated from the numerical simulations clearly demonstrates that these states are linearly stable (see colored curves in Fig. 8).

[1] C. M. Bender and S. Boettcher, Real spectra in non-Hermitian Hamiltonians having PT symmetry, *Physical*

- [2] C. M. Bender, D. C. Brody, and H. F. Jones, Complex extension of quantum mechanics, *Physical Review Letters* **89**, 270401 (2002).
- [3] C. M. Bender, Making sense of non-Hermitian Hamiltonians, *Reports on Progress in Physics* **70**, 947 (2007).
- [4] N. Moiseyev, *Non-Hermitian quantum mechanics* (Cambridge University Press, 2011).
- [5] D. Christodoulides and J. Yang, Parity-time Symmetry and Its Applications (Springer Singapore, 2018).
- [6] X. Zhang, F. Zangeneh-Nejad, Z.-G. Chen, M.-H. Lu, and J. Christensen, A second wave of topological phenomena in photonics and acoustics, *Nature* **618**, 687 (2023).
- [7] K. Kawabata, K. Shiozaki, M. Ueda, and M. Sato, Symmetry and topology in non-Hermitian physics, *Phys. Rev. X* **9**, 041015 (2019).
- [8] S. Yao and Z. Wang, Edge states and topological invariants of non-Hermitian systems, *Physical Review Letters* **121**, 086803 (2018).
- [9] J. Claes and T. L. Hughes, Skin effect and winding number in disordered non-Hermitian systems, *Physical Review B* **103**, L140201 (2021).
- [10] J. Cheng, X. Zhang, M.-H. Lu, and Y.-F. Chen, Competition between band topology and non-Hermiticity, *Physical Review B* **105**, 094103 (2022).
- [11] Q. Wang and Y. D. Chong, Non-Hermitian photonic lattices: Tutorial, *J. Opt. Soc. Am. B* **40**, 1443 (2023).
- [12] X. Zhang, T. Zhang, M.-H. Lu, and Y.-F. Chen, A review on non-Hermitian skin effect, *Advances in Physics: X* **7**, 2109431 (2022).
- [13] R. Lin, T. Tai, L. Li, and C. H. Lee, Topological non-Hermitian skin effect, *Frontiers of Physics* **18**, 53605 (2023).
- [14] N. Okuma and M. Sato, Non-Hermitian topological phenomena: A review, *Annual Review of Condensed Matter Physics* **14**, 83 (2023).
- [15] N. Hatano and D. R. Nelson, Localization transitions in non-Hermitian quantum mechanics, *Physical Review Letters* **77**, 570 (1996).
- [16] N. Hatano and D. R. Nelson, Non-Hermitian delocalization and eigenfunctions, *Physical Review B* **58**, 8384 (1998).
- [17] S. Weidemann, M. Kremer, T. Helbig, T. Hofmann, A. Stegmaier, M. Greiter, R. Thomale, and A. Szameit, Topological funneling of light, *Science* **368**, 311 (2020).
- [18] L. Zhang, Y. Yang, Y. Ge, Y.-J. Guan, Q. Chen, Q. Yan, F. Chen, R. Xi, Y. Li, D. Jia, S.-Q. Yuan, H.-X. Sun, H. Chen, and B. Zhang, Acoustic non-Hermitian skin effect from twisted winding topology, *Nature communications* **12**, 6297 (2021).
- [19] A. Maddi, Y. Auregan, G. Penelet, V. Pagneux, and V. Achilleos, Exact analogue of the Hatano-Nelson model in 1d continuous nonreciprocal systems (2023), [arXiv:2306.12223 \[physics.app-ph\]](https://arxiv.org/abs/2306.12223).
- [20] M. Brandenbourger, X. Locsin, E. Lerner, and C. Coulais, Non-reciprocal robotic metamaterials, *Nature communications* **10**, 4608 (2019).
- [21] A. Ghatak, M. Brandenbourger, J. van Wezel, and C. Coulais, Observation of non-Hermitian topology and its bulk-edge correspondence in an active mechanical metamaterial, *Proceedings of the National Academy of Sciences* **117**, 29561 (2020).
- [22] S. Liu, R. Shao, S. Ma, L. Zhang, O. You, H. Wu, Y. Jiang Xiang, T. Jun Cui, and S. Zhang, Non-Hermitian skin effect in a non-Hermitian electrical circuit, *Research* **2021**, 1 (2021).
- [23] Q. Liang, D. Xie, Z. Dong, H. Li, H. Li, B. Gadway, W. Yi, and B. Yan, Dynamic signatures of non-Hermitian skin effect and topology in ultracold atoms, *Physical Review Letters* **129**, 070401 (2022).
- [24] D. Leykam and Y. D. Chong, Edge solitons in nonlinear-photonic topological insulators, *Physical Review Letters* **117**, 143901 (2016).
- [25] F. Zangeneh-Nejad and R. Fleury, Nonlinear second-order topological insulators, *Physical Review Letters* **123**, 053902 (2019).
- [26] R. Chaunsali, H. Xu, J. Yang, P. G. Kevrekidis, and G. Theoharis, Stability of topological edge states under strong nonlinear effects, *Physical Review B* **103**, 024106 (2021).
- [27] L. Jezequel and P. Delplace, Nonlinear edge modes from topological one-dimensional lattices, *Physical Review B* **105**, 035410 (2022).
- [28] S. Kruk, Nonlinear topological photonics, in *Advances in Nonlinear Photonics*, Woodhead Publishing Series in Electronic and Optical Materials, edited by G. C. Righini and L. Sirleto (Woodhead Publishing, 2023) pp. 85–111.
- [29] X. Ni, S. Yves, A. Krasnok, and A. Alù, Topological metamaterials, *Chemical Reviews* **123**, 7585 (2023).
- [30] V. V. Konotop, J. Yang, and D. A. Zezyulin, Nonlinear waves in PT-symmetric systems, *Reviews of Modern Physics* **88**, 035002 (2016).
- [31] S. V. Suchkov, A. A. Sukhorukov, J. Huang, S. V. Dmitriev, C. Lee, and Y. S. Kivshar, Nonlinear switching and solitons in PT-symmetric photonic systems, *Laser & Photonics Reviews* **10**, 177 (2016).
- [32] S. Xia, D. Kaltsas, D. Song, I. Komis, J. Xu, A. Szameit, H. Buljan, K. G. Makris, and Z. Chen, Nonlinear tuning of PT symmetry and non-Hermitian topological states, *Science* **372**, 72 (2021).
- [33] C. Yuce, Nonlinear non-Hermitian skin effect, *Physics Letters A* **408**, 127484 (2021).
- [34] M. Ezawa, Dynamical nonlinear higher-order non-Hermitian skin effects and topological trap-skin phase, *Physical Review B* **105**, 125421 (2022).
- [35] B. Zhu, Q. Wang, D. Leykam, H. Xue, Q. J. Wang, and Y. D. Chong, Anomalous single-mode lasing induced by nonlinearity and the non-Hermitian skin effect, *Physical Review Letters* **129**, 013903 (2022).
- [36] H. Jiang, E. Cheng, Z. Zhou, and L.-J. Lang, Nonlinear perturbation of a high-order exceptional point: Skin discrete breathers and the hierarchical power-law scaling, *Chinese Physics B* **32**, 084203 (2023).
- [37] P. G. Kevrekidis, The discrete nonlinear Schrödinger equation: mathematical analysis, numerical computations and physical perspectives, Vol. 232 (Springer Science & Business Media, 2009).
- [38] D. N. Christodoulides and R. I. Joseph, Discrete self-focusing in nonlinear arrays of coupled waveguides, *Optics Letters* **13**, 794 (1988).
- [39] H. S. Eisenberg, Y. Silberberg, R. Morandotti, A. R. Boyd, and J. S. Aitchison, Discrete spatial optical solitons in waveguide arrays, *Physical Review Letters* **81**, 3383 (1998).
- [40] F. Lederer, G. I. Stegeman, D. N. Christodoulides, G. Asanto, M. Segev, and Y. Silberberg, Discrete solitons in optics, *Physics Reports* **463**, 1 (2008).
- [41] A. J. Leggett, Bose-Einstein condensation in the alkali gases: Some fundamental concepts, *Reviews of Modern Physics*

- Physics* **73**, 307 (2001).
- [42] O. Morsch and M. Oberthaler, Dynamics of Bose-Einstein condensates in optical lattices, *Reviews of Modern Physics* **78**, 179 (2006).
- [43] A. Scott, Davydov's soliton, *Physics Reports* **217**, 1 (1992).
- [44] N. Molkenhain, S. Hu, and A. J. Niemi, Discrete nonlinear Schrödinger equation and polygonal solitons with applications to collapsed proteins, *Physical Review Letters* **106**, 078102 (2011).
- [45] E. Edvardsson, J. L. K. König, and M. Stålhammar, Biorthogonal renormalization (2023), [arXiv:2212.06004](https://arxiv.org/abs/2212.06004) [quant-ph].
- [46] E. Doedel, H. B. Keller, and J. P. Kernevez, Numerical analysis and control of bifurcation problems (I): Bifurcation in finite dimensions, *International Journal of Bifurcation and Chaos* **01**, 493 (1991).
- [47] A. Dhooge, W. Govaerts, Y. A. Kuznetsov, H. G. Meijer, and B. Sautois, New features of the software MatCont for bifurcation analysis of dynamical systems, *Mathematical and Computer Modelling of Dynamical Systems* **14**, 147 (2008).
- [48] Openly accessible at: <https://sourceforge.net/projects/matcont/files/>.
- [49] For the DNLS model (HN system with $t = 1$), we mention the presence of a Pitchfork bifurcation point located at $C = 0.9036454$. At this juncture, the branch stemming from the normal mode splits into three branches. Two of these branches converge to the one-site solutions at positions $n = N/2$ and $n = N/2 + 1$ along the chain in the AC limit, with N being the size of the chain. The remaining branch reaches the two-site solution at $C = 0$. In case of the Hatano-Nelson lattice ($t \neq 1$), this Pitchfork bifurcation point undergoes a transformation into a limit point which effectively segregate these families of solutions.
- [50] D. Pelinovsky, P. Kevrekidis, and D. Frantzeskakis, Stability of discrete solitons in nonlinear Schrödinger lattices, *Physica D: Nonlinear Phenomena* **212**, 1 (2005).
- [51] E. Hairer, S. P. Nørsett, and G. Wanner, Solving ordinary differential equations I. Nonstiff problems, 2nd edition, Vol. 14 (Springer Series in Computational Mathematics, 1993).
- [52] C. Danieli, B. Many Manda, T. Mithun, and C. Skokos, Computational efficiency of numerical integration methods for the tangent dynamics of many-body Hamiltonian systems in one and two spatial dimensions, *Mathematics in Engineering* **1**, 447 (2019).
- [53] Openly accessible at: <http://www.unige.ch/~hairer/software.html>.
- [54] K. O. Rasmussen, T. Cretegny, P. G. Kevrekidis, and N. Grønbech-Jensen, Statistical mechanics of a discrete nonlinear system, *Physical Review Letters* **84**, 3740 (2000).
- [55] P. G. Kevrekidis, D. E. Pelinovsky, and A. Saxena, When linear stability does not exclude nonlinear instability, *Physical Review Letters* **114**, 214101 (2015).
- [56] M. I. Molina, Solitons in a modified discrete nonlinear Schrödinger equation, *Scientific Reports* **8**, 2186 (2018).